Rare Metal Materials and Engineering
Volume 49, Issue 6, June 2020
Available online at www.rmme.ac.cn

Science Press

Cite this article as: Rare Metal Materials and Engineering, 2020, 49(6): 1879-1884.

ARTICLE

Numerical Research on Ti-6Al-4V Strengthening Process by Laser Melt Injection of ZrO_2 Particles

Zhao Guangxi, Wei Zhengying, Du Jun, Wei Pei

Xi'an Jiaotong University, Xi'an 710049, China

Abstract: In order to improve the surface strength and heat-insulating capability of Ti-6Al-4V alloy, ZrO_2 particles were injected into the Ti-6Al-4V surface melted by laser. The melt-injection-interaction process was modeled using CFD method and the simulations were partly verified by experiments. In this model, the moving Gauss laser was defined based on the equivalent thermal effect. VOF method was adopted to analyze phase change process and detect the free surface of molten pool. The buoyancy, inertia force and viscous drag were considered when calculating the particle movements. Temperature and velocity fields inside the molten pool were analyzed, and the influences of the convection caused by thermal-fluid coupling on particles injection and distribution were revealed. The results show that the temperature field and flow field in the molten pool redistribute with the entry of the particles and the fluid flow and the solidification of the molten pool distribute the particles in different positions. The number of ZrO_2 particles was counted per 100 μm depth, and it is found that the number of the ZrO_2 particles increases first and then decreases from surface to bottom. With the increase of laser scanning velocity, particle densest positions become closer to the substrate surface.

Key words: laser melt injection; molten pool; Ti-6Al-4V

Thermal barrier coating is a class of high-temperature protective coatings which comprises a metal bonding layer and a ceramic coating surface[1,2]. Previous studies have shown that thermal barrier coatings with thickness ranging from 100 μm to 500 μm can reduce the surface temperature of high temperature alloy by 100 °C to 300 °C[3]. Currently, plasma spraying and physical gas phase deposition are the most commonly used processes to produce the thermal barrier coating[4,5]. However, the ceramic layer produced by the aforementioned processes is not strong enough since it is bonded to the substrate through an intermediate alloy layer[6]. What's more, the thermal barrier coating has the most complicated structure and the most demanding work environment compared with other kinds of coating system. For these reasons, the premature detachment problem of the thermal barrier coating is serious[7]. The LMI (laser melt injection) technique is a promising approach to solve this problem.

The LMI is an extension of laser cladding in nature, through which ceramic particles can be planted into the substrate. Since the ceramic particles are encapsulated in the alloy matrix, the possibility of shedding failure is greatly reduced[8]. LMI was studied first by Ayers[9-12], and applied US patent in 1981, Li investigated laser melt injection on aluminum alloys and found that the powder should be fed from the back side of laser beam[13]. Vreeling[14] explained that the final injection depth of the particles is controlled mainly by the temperature of the molten pool rather than by the particle velocity. Vreeling[15] found that the particles are injected over the whole depth and whole width of the melt pool. Ocelik[16] observed the orientation relationship between ceramic particles and phase formed in the reaction zone by transmission electron microscopy and by EBSD. Obadele[17] studied the relationships between laser speed, structure and tribocorrosion properties of the synthesized composite coatings. Most of the researches studied this process using experimental methods since it is more accurate and perceptual intuitive. However,

Received date: June 25, 2019
Foundation item: National Key Research and Development Project (2017YFB1103201)
Corresponding author: Wei Zhengying, Ph. D., Professor, School of Mechanical Engineering, Xi'an Jiaotong University, Xi'an 710049, P. R. China, Tel: 0086-29-82665987, E-mail: zywei@mail.xjtu.edu.cn

Copyright © 2020, Northwest Institute for Nonferrous Metal Research. Published by Science Press. All rights reserved.

experiment methods are also expensive and time-consuming, and it is difficult to observe phenomena inside. As a result, numerical simulation is also an effective approach to study the LMI process. Ti alloys exhibit excellent material properties such as good fatigue, high strength to weight ratio and good toughness. However, poor wear resistance hampers many potential applications. So, this paper researched Ti-6Al-4V (TC4) with a coating against high temperature and high wear conditions.

1 Mathematical Model

Schematic diagram of LMI process is shown in Fig.1, laser beam and the powder feeder move at the same speed. Under the thermal effect of high-energy laser, TC4 substrates begin to melt rapidly. Simultaneously, ZrO_2 powders are injected into the molten pool and interact with the liquid metal including heat transfer and flow, and their positions are finally determined after solidification of the molten pool. As a result, an insulation layer of ZrO_2 particles is formed on the substrate surface.

Laser beam is the heat source of the whole LMI process which is usually treated according to their equivalent thermal effect in mathematic model. Gaussian surface heat source distribution is shown in Eq.(1)[18]:

$$q(r)=\frac{Q}{2\pi\sigma_q^2}\exp\left(-\frac{r^2}{2\sigma_q^2}\right) \tag{1}$$

where q(r) represents the heat flux, σ_q is the Gaussian heat source distribution parameters, Q is heat input rate, r is the distance from the center of heat source.

Gauss body heat source is shown in Eq.(2)[19]:

$$q(x,y,z,t)=\frac{3c_sQ}{\pi H\left(1-\frac{1}{e^3}\right)}\cdot \exp\left[\frac{-3c_s}{\log\left(\frac{H}{z}\right)}\left(x^2+y^2\right)\right] \tag{2}$$

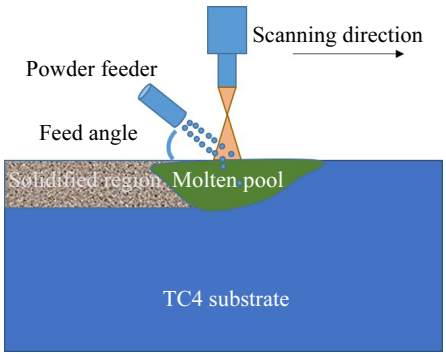

Fig.1 Schematic diagram of LMI process

where $C_s=3/R_0^2$, R_0 is the heat source radius, H is the height of heat source from the substrate.

Surface heat source form may have a big deviation for high energy beam welding (such as laser welding and electron beam welding), because it does not take penetration into consideration[20,21]. Therefore, this paper uses the body heat source equation instead of the surface one.

Moving items are added to the stationary Gaussian heat source equation (2) to make the laser beam move along the preset trajectory. Eq. (2) is modified to move along the y axis based on the characteristics of the Gaussian equation.

Flow-3D allows its users to customize their simulation process by programming in Fortran language, and Flow-3D is used to create the model in this paper. The basic idea of customization is to keep tracking on the free surface of the molten pool and to impose the moving heat source expressed in Eq. (3) on it.

The numerical simulation of the molten pool uses the following assumptions[22]:

1) It is incompressible Newtonian fluid in the molten pool, and it flows in laminar flow form.

2) This paper only considers gravity, buoyancy and surface tension as driving forces of the fluid flow.

3) Mushy zone is treated as an isotropic permeability of porous medium.

4) Substrate is homogeneous isotropic material.

VOF method[23,24] is used to track the free surface. Governing equations for incompressible Newtonian fluid are given as below:

$$\nabla\cdot\vec{V}=0 \tag{3}$$

where ∇ is the gradient operator, $\vec{V}$ is the velocity of the fluid. The conservation equation is based on fluid fraction (F) of grid cell volume, F=1 denotes that the grid cell is full of fluid, while F=0 represent the grid cell is full of solid, besides, 0<F<1 means it contains a free surface in the grid volume.

$$\frac{\mathrm{d}F}{\mathrm{d}T}=\frac{\partial F}{\partial t}+\nabla\cdot\left(\vec{V}F\right)=0 \tag{4}$$

Phase change problem of substrate melting is processed according to the relationship of enthalpy (h) and temperature. The calculation equation of h is given in Eq.(5):

$$h=\begin{cases}\rho_sT_sC_s & T<T_s\\ h(T_s)+h_{sl}\dfrac{T-T_s}{T_l-T_s} & T_s\leqslant T\leqslant T_l\\ h(T_l)+\rho_lC_l(T-T_l) & T_l<T\end{cases} \tag{5}$$

where T represents the temperature, ρ_s is the density of the solid phase, T_s is the temperature of solid phase, C_s is the specific heat of solid phase, and ρ_l is the density of the liquid phase, T_l is the temperature of liquid phase, C_l is the specific heat of liquid phase.

Latent heat of fusion refers to absorbed or released heat when the phase of material changes from solid to liquid or from liquid

to solid, which is very important for phase change analysis and cannot be neglected. Physical parameters of TC4 are listed in Table 1 based on papers of Aiqin[25] and Yang[26].

The surface tension is a significant contributor when modeling Marangoni effect-based flow and is seldom available through experimental methods. Surface tension (γ) of TC4 is 1.6411 N/m at melting temperature, and it decreases with temperature rise. Relationship of changing rate with temperature is:

$$\frac{d\gamma}{dT} = -0.00028 \text{ N/(m} \cdot \text{K)} \quad (6)$$

In this paper laser power density is 283 W/mm^2, spot diameter of which is 3 mm. The method for solving particle generation is based on the discrete particle method. Particles are created by sampling randomly from assumed probability distributions that govern particle properties at injection nozzle, i.e., position, size and velocity. ZrO_2 particles is assumed to be ideal spherical, the diameter of them is 60 μm, feeding rate is 85 mg/s and feeding angle is 35°. The moving speed of the laser and the particle feeder are both 0.01 m/s.

2 Results and Discussion

2.1 Effect of particles on the flow field and temperature field of the molten pool

As is shown in Fig.2 and Fig.3, temperature field and velocity vector of molten pool are calculated with and without particle injection, respectively when t=0.05 s.

Apparently, the velocity vector points are from the heat source center to around in Fig.2a. This is because the temperature of laser spot center is higher, the surface tension decreases with temperature increasing, and fluid flows from the lower surface tension region to higher surface tension region. From Fig.2b and Fig.2c we find that two circulations form in the molten pool due to the effects of both buoyant flow which occurs due to density changes and Marangoni convection. Besides, the two circulations of Fig.2c are symmetrical.

Comparing Fig.3 with Fig.2, velocity field of molten pool is

Table 1 Physical properties of TC4

Melting point/K	Solidifying point/K	Viscosity/ kg·(m·s)$^{-1}$	Solid phase heat conductivity/J·(m·s·K)$^{-1}$	Liquid phase heat conductivity/J·(m·s·K)$^{-1}$	Latent heat/ kJ·kg^{-1}
1928	1878	0.0029	5.4	15.9	392

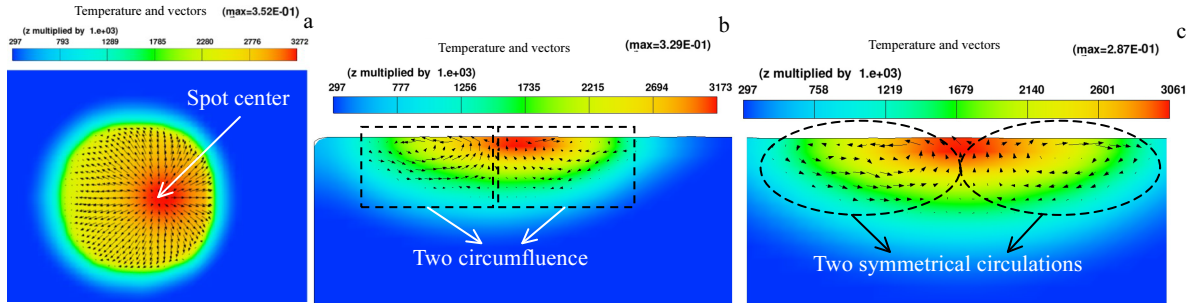

Fig.2 Temperature field and velocity vector of molten pool without particle injection: (a) substrate surface, (b) section parallel to laser moving direction, and (c) section perpendicular to laser moving direction

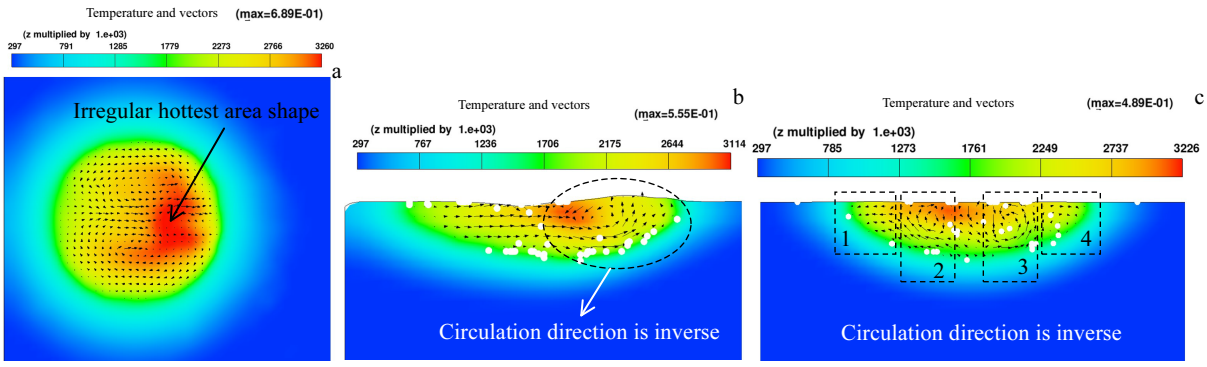

Fig.3 Temperature field and velocity vector of molten pool with particle injection: (a) substrate surface, (b) section parallel to laser moving direction, and (c) section perpendicular to laser moving direction

disturbed by particles. Since particles have positive velocity components along laser moving direction and along gravity direction, magnitude of fluid velocity along these two directions increases. As a result, the velocity vector on the substrate surface is no longer point from the laser spot center to around, and the shape of the hottest area becomes irregular. As is shown in Fig.3b, velocity field along laser moving direction has only one circulation whose direction is inverse compared with Fig.2b. It is found that there are still two circulations (area 2 and 3) in Fig.3c, but the velocity direction is inverse compared with Fig.2c, too. The influences of particle disturbances are smaller at the edge of the molten pool; therefore, the velocity direction of area 1 and 4 is identical with Fig.2c. The maximum velocity of Fig.2a, 2b, 2c, Fig.3a, 3b and 3c are 0.352, 0.329, 0.287 and 0.689, 0.555, 0.489 m/s, respectively. The maximum temperature of Fig.2a, 2b, 2c, Fig.3a, 3b and 3c are 3272, 3173, 3061 and 3260, 3114, 3226 K, respectively. Through data post-processing, we find the maximum depth of molten pool is 0.77 mm, and the length is 2.5 mm.

2.2 Experimental verification and particle distribution

Experiments were conducted under the same condition with the simulation. The solid fraction of the central cross-section of the molten pool is shown in Fig.4a, and the cross-section morphology of test piece is shown in Fig.4b. Length and depth of the molten pool in Fig.4b are measured, and the values are 2.7 and 0.76 mm, respectively.

As it is mentioned in subsection 2.1, the length and depth of the molten pool in Fig.4a are 0.77 and 2.5 mm, respectively. Comparing Fig. 4a with Fig.4b, length-depth ratio of Fig.4a is 3.25, while it is 3.42 in Fig.4b. Therefore, the length-depth ratio error is 4.97%, while the length and depth errors of molten pool are 7.4% and 1.3%, respectively. In order to verify the accuracy of the model, tangent angles at the depth of 0.4 mm (angle 1 and 3) and 0.5 mm (angle 2 and 4) were measured by Auto CAD. The values of angle 1 and 3 are 39° and 38°, respectively, so the error is 2.6%. The values of angle 2 and 4 are 22° and 21°, respectively, so the error is 5%. Therefore, the simulation results are credible to a certain extent.

Strong convection caused by heat distribution and particles injection transport the particles to different positions. After solidification of the molten pool, the locations of the ZrO_2 particles are finally settled. Three-dimensional view of particles distribution is shown in Fig.5. It can be seen that the number of particles at the right side is more than the left at the initial location, which is mainly because particles have a positive velocity component along right direction. Since the model calculation is too large, the subsequent results are not calculated, but it can be predicted that particles would distribute uniformly at the following position.

The number of ZrO_2 particles per 100 μm depth was calculated out at 0.1. The number of particles is 806, 1086, 1248, 1117, 900, 559 and 231. It is found that the depth within 300 μm to 400 μm has the greatest number of particles. Fig.6 shows the relationship between the particle numbers and the depth of molten pool; ZrO_2 particle number increases first and then decreases with increasing the depth of molten pool. This is because convection flow within the inner region of the molten pool is much stronger than the edge position, and the density of ZrO_2 is larger than that of TC4.

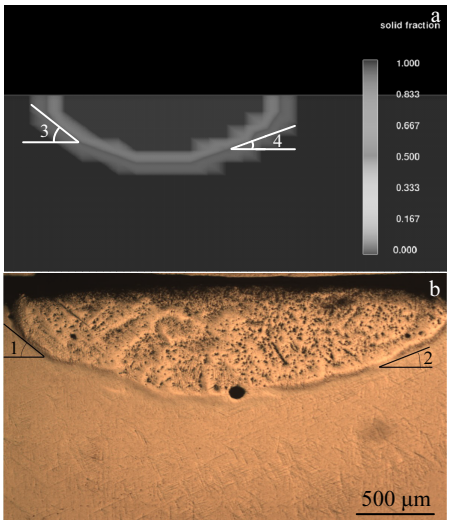

Fig.4 Solid fraction of the center cross-section of the molten pool (a) and section morphology test piece (b) perpendicular to laser moving direction

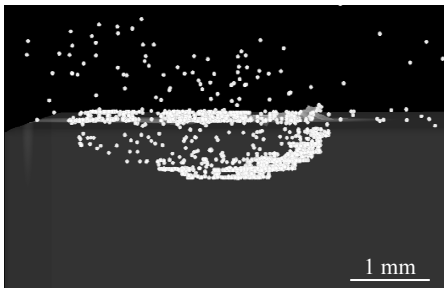

Fig.5 Three-dimensional view of particles distribution

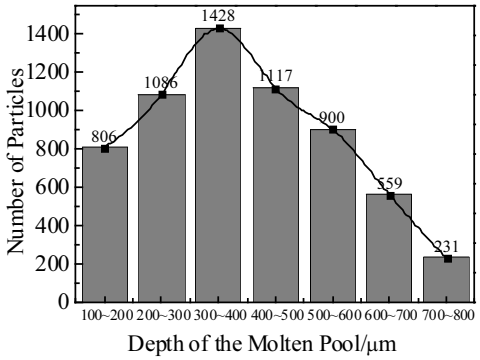

Fig.6 Number of particles at different depth

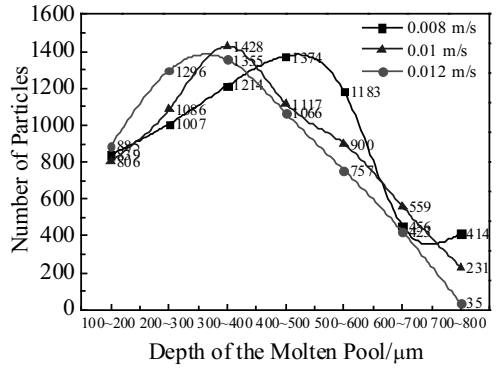

Fig.7 Particles distribution at different laser scanning velocity

The influence of laser scanning velocity on particles distribution was studied in this paper. The number of ZrO_2 particles per 100 μm depth was compared at different velocity: 0.008, 0.01, 0.012 m/s and is shown in Fig.7.

It is easy to understand that when the laser scanning speed increases, the energy absorbed per unit area of the substrate reduces so that the size of the molten pool reduces. As a result, with the increase of laser scanning velocity, particle densest distribution positions become closer to the substrate surface. The depth range from 700 μm to 800 μm has the most particles at the velocity v=0.008 m/s. It is because when other conditions are the same (including total heat input, initial particle velocity and heat dissipation etc.), the smaller the laser scanning speed, the longer the solidification time of the molten pool will be. Therefore, the particles have more time to sink into the bottom of the molten pool at v=0.008 m/s.

Since the particles number in the whole three-dimensional molten pool can not be observed by experimental method, this paper verifies the numerical results by comparing the particles number in the central cross-section of the molten pool. The number of particles were counted by the metallographic microscope after metallographic treatment. The number of particles in three central cross-sections of the molten pools at 0.1 s was counted and the results are 211, 225, 246, while the numerical result is 248. As a result, the error between the numerical result and the average experimental result is 9.1%.

3 Conclusions

1) Without particles injection two circulations form in the molten pool due to buoyant flow and Marangoni convection.

2) The particles number of the molten pool from surface to bottom increases first and then decreases.

3) With the increase of laser scanning velocity, particle densest positions become closer to the substrate surface.

References

1 Clarke D R, Oechsner M, Padture N P. *MRS Bulletin*[J], 2012, 37(10): 891

2 Zhao Santuan, Zhang Xiangzhao, Liu Guiwu *et al*. *Rare Metal Materials and Engineering* [J], 2018, 47(3): 759

3 Zhang Gang, Liang Yong. *Journal of Shenyang Institute of Techndogy*[J], 2000, 19(1): 1 (in Chinese)

4 Jamali H, Mozafarinia R, Shoja-Razavi R *et al*. *Journal of the European Ceramic Society*[J], 2014, 34(2): 485

5 Ahmadi-Pidani R, Shoja-Razavi R, Mozafarinia R *et al*. *Materials & Design*[J], 2014, 57: 336

6 Rajasekaran J, Gnanasekaran B M, Senthilkumar T *et al*. *International Journal of Research in Engineering and Technology*[J], 2013, 2(7): 240

7 Patel N V, Jordan E H, Sridharan S *et al*. *Surface and Coatings Technology*[J], 2015, 275: 384

8 Pei Y T, Ocelik V, De Hosson J T M. *Acta Materialia*[J], 2002, 50(8): 2035

9 Ayers J D, Tucker T R. *Thin Solid Films*[J], 1980, 73(1): 201

10 Ayers J D. *Thin Solid Films*[J], 1981, 84(4): 323

11 Ayers J D, Schaefer R J, Robey W P. *JOM*[J], 1981, 33(8): 19

12 Ayers J D. *Wear*[J], 1984, 97(3): 249

13 Li F Q, Li L Q, Chen Y B. *Surface Engineering*[J], 2013, 29(4): 296

14 Vreeling J A, Ocelık V, Pei Y T *et al*. *Acta Materialia*[J], 2000, 48(17): 4225

15 Vreeling J A, Ocelik V, De Hosson J T M. *Acta Materialia*[J], 2002, 50(19): 4913

16 Ocelik V, Vreeling J A, De Hosson J T M. *Journal of Materials Science*[J], 2001, 36(20): 4845

17 Obadele B A, Lepule M L, Andrews A *et al*. *Tribology International*[J], 2014, 78: 160

18 Liu Chuan, Zhang Jianxun, Niu Jing. *Rare Metal Materials and Engineering*[J], 2009, 38(8): 1317

19 Gu J C, Tong L G, Li L *et al*. *Materials Review* [J], 2014, 28(1): 143 (in Chinese)

20 Kim M S, Jo S E, Ahn H R *et al*. *Smart Materials and Structures*[J], 2015, 24(6): 65 032

21 Kaplan A. *Journal of Physics D: Applied Physics*[J], 1994, 27(9): 1805

22 Arumugam Selvi A. *Dissertation for Master*[D]. Columbus: The Ohio State University, 2014

23 Li Q, Ouyang J, Yang B *et al*. *Applied Mathematical Modeling*[J], 2012, 36(5): 2262

24 Li Suli, Wei Zhengying, Du Jun *et al*. *Rare Metal Materials and Engineering*[J], 2017, 46(4): 893

25 Aiqin D, Li C. *Proceedings of the 36th International MATADOR Conference*[C]. London: Springer, 2010: 591

26 Yang M, Yang Z, Cong B *et al*. *Welding Journal*[J], 2014, 8: 312

Ti-6Al-4V 基体激光植入 ZrO_2 颗粒工艺过程数值分析

赵光喜，魏正英，杜　军，魏　培

(西安交通大学，陕西 西安 710049)

摘　要：为了提高 Ti-6Al-4V 合金零部件的表面强度及耐热性能，在利用激光熔化后的 Ti-6Al-4V 材料表面上植入 ZrO_2 陶瓷颗粒。基于 CFD 计算方法建立了三维瞬态激光植入工艺过程数值分析模型并对部分实验结果进行了验证。该模型根据等效热效应对移动激光热源进行计算，利用 VOF 方法追踪流体的自由表面。考虑浮力、惯性力、粘性阻力对颗粒运动的影响分析了颗粒在熔池内的运动过程，对比分析了是否添加颗粒 2 种工况下熔池内的温度场与流场分布。结果表明，颗粒的进入使得熔池内温度场与流场重新分布，流体的流动和熔池的凝固使颗粒分布于不同位置。通过对每 100 μm 深度上熔池不同位置处的颗粒数进行统计发现，熔池中颗粒数从表面到底部先增加后减小。随着激光扫描速率的增加，颗粒最密集位置越来越靠近熔池表面。

关键词：激光植入；熔池；Ti-6Al-4V 合金

作者简介：赵光喜，男，1989 年生，博士，西安交通大学机械工程学院，陕西 西安 710049，电话：029-82665987，E-mail: zgx6464946@gmail.com